SUPPLEMENTARY INFORMATION

The patchwork loess of Central Asia: Implications for interpreting aeolian dynamics and past climate circulation in piedmont regions

Aditi K. Dave[1,2*], Lenka Lisá[3], Giancarlo Scardia[4], Saida Nigmatova[5], Kathryn E. Fitzsimmons[1,2]

[1]*Research Group for Terrestrial Palaeoclimates, Max Planck Institute for Chemistry, Mainz, Germany*
[2]*Department of Geosciences, University of Tübingen, Schnarrenbergstrasse 94-96, 72076 Tübingen, Germany*
[3]*Institute of Geology, Czech Academy of Sciences, Prague, Czech Republic*
[4]*Instituto de Geociências e Ciências Exatas, Universidade Estadual Paulista, 13506-900 Rio Claro SP, Brazil*
[5]*Institute of Geological Sciences K. Satpaeva, Ministry for Education and Science of the Republic of Kazakhstan, Almaty, Kazakhstan*
**Present Address*

1. Optically Stimulated Luminescence (OSL) dating

1.1. Sample preparation

All the samples were processed and measured under subdued red-light conditions at the Institute of Geosciences, Johannes Gutenberg University and the Max Planck Institute for Chemistry (MPIC) in Mainz, Germany. Different grain size fractions were extracted by wet-sieving. However due to the lack of sufficient coarse grains (>45 µm), fine grain (4-11 µm) samples were prepared for OSL analysis using established protocols (Frechen et al., 1996). For the preparation of fine grain (4-11 µm) fraction – the <63 µm sediment was treated with 10% HCl followed by 10% H_2O_2 to remove carbonates and organics respectively. The sediment was then treated with 0.1N sodium oxalate to remove clays. The 4-11 µm polymineral fraction was obtained from the bulk fraction (<63 µm) by settling using Stokes Law. This polymineral fine grain fraction was treated with 37% Hexafluorosilicic acid (H_2SiF_6) for 7 days to remove feldspar and washed with 10% HCl to remove fluoride precipitates to obtain fine grained (4-11 µm) quartz rich fraction (Jackson et al, 1976). All aliquots were prepared by depositing a suspension of 4-11 µm quartz fraction using acetone on 9.7 mm stainless steel discs. The purity of the quartz extracts for all samples was verified by the near background signal observed on IR stimulation of the sample after a given dose (c.19 Gy) for all the samples (Duller, 2003).

1.2. Luminescence Measurements

All luminescence measurements were made using an automated Risø TL-DA-20 reader equipped with a $^{90}Sr/^{90}Y$ beta sources (Thomsen et al., 2006) calibrated to a dose rate of 0.095 ± 0.02 Gy/s. The sample was stimulated using IR LED (870 ± 30 nm, 300 mW/cm^2) and blue LED (470±30 nm, 80 mW/cm^2) and the emitted luminescence signal was detected by by EMI 9235QA photomultiplier tube fitted with a 7.5 mm Hoya U-340 and a combination of Schott BG-39 and BG-3 filters to detect quartz and feldspar emissions respectively.

1.2.1. OSL dating of quartz

The natural and regenerative OSL decay curves obtained from fine-grained quartz from all five sites are sufficiently bright for reliable dating, although the intensity varies between samples. The generally high sensitivity observed in our samples contrasts with observations from sites further east in the Ili Basin (e.g., Li et al., 2018). The fine-grained quartz OSL decay curves show rapid decay within the initial 1 s of stimulation, indicating dominance of the rapidly bleached fast component (Fig. S2), and are suitable for luminescence dating.

Prior to any luminescence measurements, the thermal stability of the signals for equivalent dose (D_e) determination was tested using the preheat plateau tests. The tests were performed on three discs each of two samples, A0021 and A0034, from profile PAN and ASH respectively at 180, 220, 240, 260 and 280^{o}C (Fig. S3a). The results indicate an acceptable preheat plateau range between 240 to 260^{o}C, hence a preheat of 260^{o}C with a cut heat of 240^{o}C for 10s was chosen for equivalent dose measurements in all fine grain quartz samples.

In order to negate any suspicion of feldspar contamination to the quartz-dominant OSL signal, an additional IR stimulation was added prior to every blue stimulation in the classic Single Aliquot Regenerative protocol (SAR; Murray and Wintle, 2000, 2003) - commonly referred to as DSAR (or Double-SAR; Banerjee et al, 2001). This approach was developed and commonly applied to obtain quartz-dominated post-IR OSL signal from a feldspar contaminated or polymineral fraction (Banerjee et al., 2001; Roberts and Wintle, 2001; Jain and Singhvi, 2001). Some studies have previously reported discrepancies between the D_e values evaluated from polymineral post IR-OSL signal compared to that from chemically purified quartz OSL signal (Zhang and Zhao, 2007; Zhang et al., 2007), which was related to IR exposure time and bleaching temperature utilised prior to blue stimulation in the DSAR protocol. Since in our study, we apply the DSAR protocol on pure quartz-rich grains, we do not expect any such discrepancy. Nevertheless, we optimise the performance as well as verify the applicability of the DSAR protocol on our samples by comparing the D_e obtained from a simple SAR protocol and that obtained from the DSAR protocol (at different IR bleaching times and temperatures) on a selected fine grain quartz sample (A0034).

Three discs each of sample A0034 was run for a combination of two different IR bleaching temperatures (50^{o}C and 70^{o}C) with two different IR bleaching times (40s and 100s) in the DSAR protocol (Table S3). The results obtained from these tests along with that obtained from running a simple SAR protocol are summarised in Fig.S3b. These results (as also observed by Zhang and Zhao, 2007) show that short IR exposure times of 40 to 100s seconds do not have much impact on the D_e's, however it seems that a lower IR bleaching temperature of 50^{o}C is more suitable for the application of the DSAR method to our samples. Hence, an IR stimulation of 100s at 50^{o}C was chosen for all D_e measurements using DSAR protocol. To further check the applicability of the DSAR protocol, dose recovery tests was performed on 3-5 discs each of sample A0025 (PAN) and A0034 (ASH) using the DSAR (with an IR stimulation at 50^{o}C for 100s) and a simple SAR protocol. After bleaching the samples with Blue LEDs at room temperature

for 80s, a radiation dose of c.47.5 Gy (close to their corresponding equivalent dose) was given to the samples. This laboratory dose was then measured using the SAR and DSAR protocol for both the samples and the resulting ratio of recovered laboratory dose to given dose was found to be within 10% of unity for both the samples irrespective of the applied protocols (Fig. S3c). This further affirms the suitability of the DSAR protocol for age determination of fine grain samples for our samples.

D_e was determined from 16-22 aliquots each, of 19 fine grained quartz samples from four sites using the DSAR protocol (Table 1). The steps of the DSAR protocol are listed in Table S3. The robustness of the DSAR protocol on individual aliquots is tested with a set of intrinsic performance steps (recycling and recuperation) included after all the irradiation steps in every measurement. The recycling ratio (ratio of repeated dose to corresponding regenerative dose) was found to be within 10% of unity for all samples. While the recuperation ratio was <2% of the natural OSL signal for all aliquots, suggesting negligible thermal transfer of charge during OSL measurements. The dose response curves for all samples were fitted with a single saturating exponential function to obtain the best fit based on reduced chi square parameter. The early and late background subtraction method (Cunningham and Wallinga, 2010) for D_e determination was tested for all samples and no apparent change in D_e value was observed. Hence, we utilise the initial 0.8 s after subtracting the last 8s from the background OSL signal for calculation of the net OSL signal from each aliquot. The Central Age Model (Galbraith et al., 1999) was used to calculate the D_e for all samples.

Initial application of DSAR protocol on sample A0003 (site TAU, depth = 1 m) and A0038 (site MAL, depth = 1m) exhibited a flattening of the quartz OSL dose response curve indicating a near saturation of the quartz in nature. However, Timar-Gabor et al (2017) observed that the SAR dose response curve (DRC) constructed from the OSL fast component of fine grain quartz was described by a sum of two saturating exponential function and did not undergo saturation at high doses (>10000 Gy), even though it may have attained saturation with respect to its limit for dating under natural conditions. In order to ascertain that the quartz in our samples was in saturation and evaluate its saturation limit, we constructed the DRCs with a high dose range (c. upto 1500 Gy) for selected samples from the top and bottom of the profiles at site TAU (A0003, depth=1.5m; A0016, depth=7m) and MAL (A0037, depth=1m; A0050, depth=5.1m) respectively (Fig. S4). All four samples, yield an 'apparent' equivalent dose estimate of c.180-190 Gy (c.70 ka), which corresponds to the natural saturation values of fine grain quartz in this region (Table 1 and Fig. S4).Therefore all samples, below 1.5 m depth at TAU and below 1 m at MAL exhibit natural saturation (not laboratory) of the OSL quartz signal.

1.2.1. pIRIR dating of polyminerals

In cases where apparent natural saturation of the fine-grained quartz-OSL signal was observed, elevated temperature post-infrared infrared stimulated luminescence (pIR-IRSL) dating of polymineral fine grains was undertaken (protocol outlined in Table S3; Theil et al, 2011). Based on the observations made by Thomsen et al (2008) and Murray et al (2009) and following the

work of Theil et al (2011), a pIR-IRSL protocol, with a preheat of 320°C for 60 s, followed by an IR stimulation at 50°C for 200s (IR_{50}) and subsequent measurement of the pIR-IRSL signal at 290°C for 200 s ($pIRIR_{290}$) was employed for all polymineral fine grain samples. A high temperature bleach at 325°C for 100 s was performed after each cycle to remove any residual charge. The D_e was evaluated using the net signal obtained from the initial 2.4 s of stimulation after subtraction of the background from the last c. 20 s. Since initial D_e measurements yielded a high natural dose, we constructed dose response curves extending over a high dose range (upto c. 3325 Gy, after Buylaert et al., 2012) to evaluate the D_e from polymineral fine grains. We performed this analysis on 3 aliquots each of the same set of samples from TAU (A0003 and A0016) and MAL (A0038 and A0050) as used in the quartz saturation experiment. The results are summarised in Fig. S5a,b. We assessed the closeness of the natural pIRIR signal to saturation by taking a ratio of the sensitivity corrected natural pIRIR signal to that obtained at c. 3225 Gy (Fig. S5c; after Avram et al., 2020). The D_e's of all the samples fall between 88-92%, which is greater than $2D_o$. D_o refers to the characteristic dose obtained from the exponential function used to fit the dose response curve and $2D_o$ refers to the dose value defined as 85% of maximum intensity for quartz OSL signal (Wintle and Murray, 2006). The $2D_o$ value is recommended as the upper limit for quartz OSL dating as any uncertainty in the natural signal leads to a higher asymmetric uncertainty in the evaluated D_e values (Wintle and Murray, 2006). Since, no such equivalent criteria exists for pIRIR signals, we evaluate our samples based on the same criteria as quartz OSL. Therefore, the $pIRIR_{290}$ ages from TAU and MAL are considered as minimum ages and are summarised in Table S2.

1.3. Dose rate calculations

Environmental radiation dose rates were calculated from the U, Th and K concentrations obtained from bulk sediment samples using high resolution gamma spectrometry. Radionuclide concentrations were converted to dry dose rates using conversion factors of Guerin et al. (2011). The in-situ moisture in the samples varied between 5-12% and the saturated water content varied between 15-25% for all sample, hence the dose rates for all the samples were attenuated for moisture using in-situ water content of 10 ± 5%. The cosmic ray component of the dose rates was determined from sample depths and uniform values for sediment density and site altitude, latitude and longitude, following Prescott and Hutton (1994). An alpha efficiency value (a-value) of 0.038 ± 0.002 for fine grained quartz and 0.086 ± 0.004 for poly mineral fine grains was utilised for all calculations (Rees-Jones, 1995). Given the size of fine grains (4-11), the contribution of internal alpha activity to dose rate is assumed to be negligibly small and ignored for all calculations. All dose rate calculations were performed using DRAC v.1.2 (Durcan et al., 2015). The radionuclide activities of U and Th were evaluated for possible disequilibrium and the results are presented in Table S5 and discussed in section 1.3.2.

1.3.1. Water content of loess samples

The measured water content of most samples from the study sites varies from 5-12%. The sampling for luminescence dating samples was done during the summer of 2017 and there is a possibility that the measured *in situ* water content from the samples are underestimated due to evaporation following the cleaning of the section and storage of the samples. Water saturation experiments performed on sediments from the study sites suggests a maximum water saturation of 20±5 %. Hence, we utilise a water content of 10±5% for all our dose rate calculations (Buylaert et al., 2015; Li et al., 2016b).

1.3.2. Disequilibrium

The radionuclide activities ($Bq.kg^{-1}$) and daughter to parent ratios obtained by high resolution gamma spectrometry of ^{238}U and ^{232}Th decay chains from all the samples are summarised in Table S5. We investigate the secular disequilibrium assumption in the ^{238}U decay chain by assessing the ratio of the activity concentrations of ^{210}Pb to ^{226}Ra. ^{210}Pb:^{226}Ra activity ratios indicate long term in-situ loss of ^{222}Rn during burial time. The gamma dose rate for all the samples in this study was calculated assuming secular equilibrium. If the level of disequilibrium, as seen in the activity ratios of c.0.8 for ^{210}Pb:^{226}Ra in Table S5 had existed throughout the burial period, then the total dose rate would be c.2% lower than the ones calculated here (based on Olley et al, 1996). Such a change in dose rate would not affect the ages significantly and would be consistent within a 2σ error limit.

2. Assumptions and Considerations: Age-depth modelling and mass accumulation rates

2.1. Optical ages for age depth modelling

A total of 33 loess sites, 14 sites from the Ili basin (including 3 sites from this study), 8 sites from other neighbouring basins in Arid Central Asia (ACA) and 11 representative sites from the Chinese loess Plateau (CLP) were chosen for this study. Table S6 contains a summary of the sites evaluated in this study as well as the references from where the optical ages have been obtained. To ensure a meaningful and robust comparison of MAR between the sites, only sites with a high resolution (≤ 1.5 m) absolute chronology were selected. Luminescence ages based on quartz OSL and feldspar pIRIR signal were evaluated for a period of 60-0 kyr. We did not consider any luminescence ages based on IR_{50} signal as well as any radiocarbon ages for purposes of age-depth modelling.

2.2. Bacon modelling parameters

Bayesian age depth modelling was performed using R package Bacon (Blaauw and Christen, 2011) using optical ages from various sites summarised in Table S6. Bacon uses Bayesian statistics to reconstruct accumulation histories for deposits by combining absolute ages with prior information like accumulation rate and its variability over time (memory, derived from autocorrelation). Inverse accumulation rates (sedimentation times, $yrs.cm^{-1}$) are estimated

from millions of Markov Chain Monte Carlo (MCMC) iterations, and these rates form the age depth model. Th Inverse accumulation rates are controlled by prior information which have been set with default values: accumulation shape = 1.5 and accumulation mean = 20 for the gamma distribution and memory mean =0.7 and memory strength =4 for beta distribution, that describe the memory effects or autocorrelation of the inverse sedimentation rates. The thickness parameter in bacon is set as 10 or 20 depending on the length of the profile being analysed. In cases where hiatuses have been identified by the authors in the respective publications, then these hiatuses were specified at given depths in the model. In case of hiatuses >10 ka years, the bacon model was run to get individual age vs depth model for each section within the site.

The resulting modelled depths and weighted mean ages from the Bacon-derived age-depth models were used to evaluate sedimentation rates ($cm.ka^{-1}$; SR) according to the equation:

$SR = (d_2-d_1)/(t_2-t_1)$

where d_2, d_1 and t_2, t_1 refer to consecutive depths and corresponding modelled mean ages respectively.

Comparison of past dust records from different loess deposits with each other and with other global dust flux records from ice cores and ocean sediments requires the evaluation of loess mass accumulation rates (MAR, $gm^{-2}a^{-1}$), which are computed using the equation:

$MAR = SR \times \rho_{dry} \times f_{eol}$

where SR refers to sedimentation rate (m/a), ρ_{dry} is the dry bulk density (gm^{-3}) and f_{eol} refers to the sediment fraction that is aeolian in nature (Kohfield and Harrison, 2000); $f_{eol} = 1$ for all calculations, since we assume that loess is almost entirely aeolian in nature. Dry bulk density for sediments varies with nature of sediment, depth and grain size; the systematic use of these parameters in previously published literature is based on approximate estimates from the region or on values from neighbouring loess sites. Furthermore, information on down-section variation of dry bulk density in loess is sparse and usually a constant value is assumed for an entire profile. In all the sites evaluated in this study, most studies use dry bulk density values based on approximate regional estimates, which vary from 1.2 gcm^{-3} (in palaeosols) upto 1.8 gcm^{-3} (in loess) depending on the site and region (ACA: Jia et al., 2018; Wang et al., 2019; Li et al., 2019b; CLP: Kohfeld and Harrison, 2003). This variation can alone add an uncertainty of upto 20% to the MAR values at the site. We keep this in mind while drawing conclusions based on comparison of MAR's between different sites.

Sites where, high deposition occurs during short time intervals (e.g. XEBLK-Li et al, 2016, ASH-this study) can lead to a modelled dataset with high frequency variations (noise) around the mean value. In such cases for simplicity and better representation, we use a 10-point running average through the dataset. Our evaluation of MAR's from luminescence ages for most sites agrees (1σ uncertainty) with that evaluated by the respective authors of the original work. The differences (where applicable) occurs due to the statistical approach utilised for age-depth modelling.

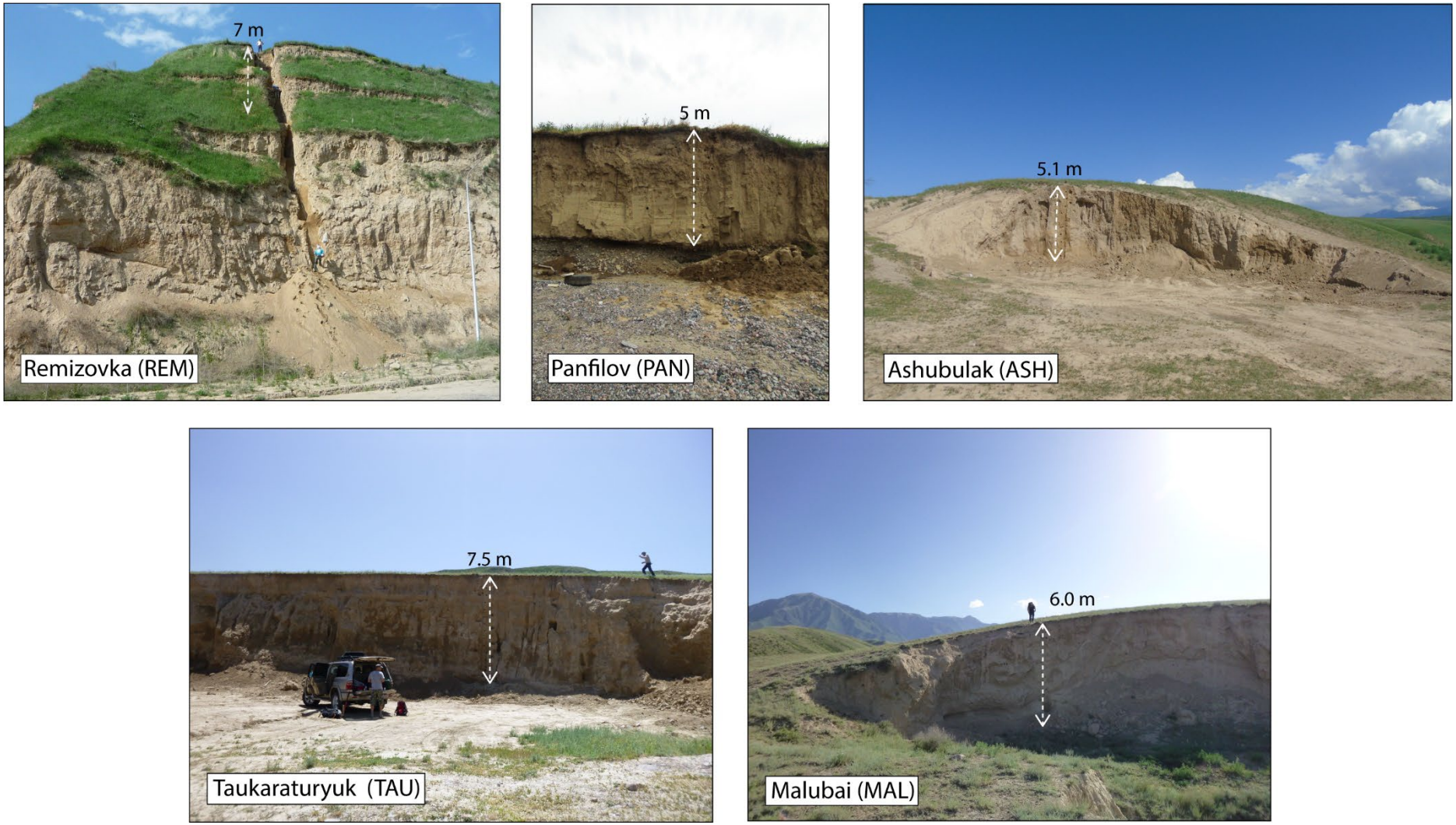

Fig. S1. Loess sites under study in the Ili basin of SE Kazakhstan.

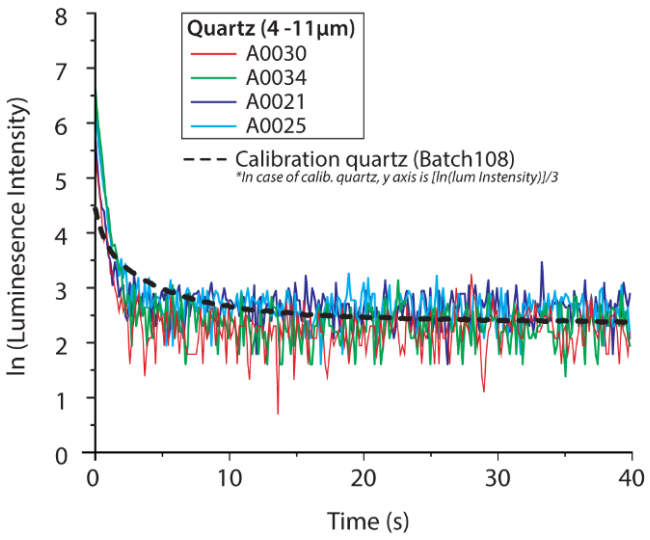

Fig. S2. Comparison of quartz OSL signal behaviour of fine grain calibration quartz with that from Central Asian loess sites, PAN and ASH.

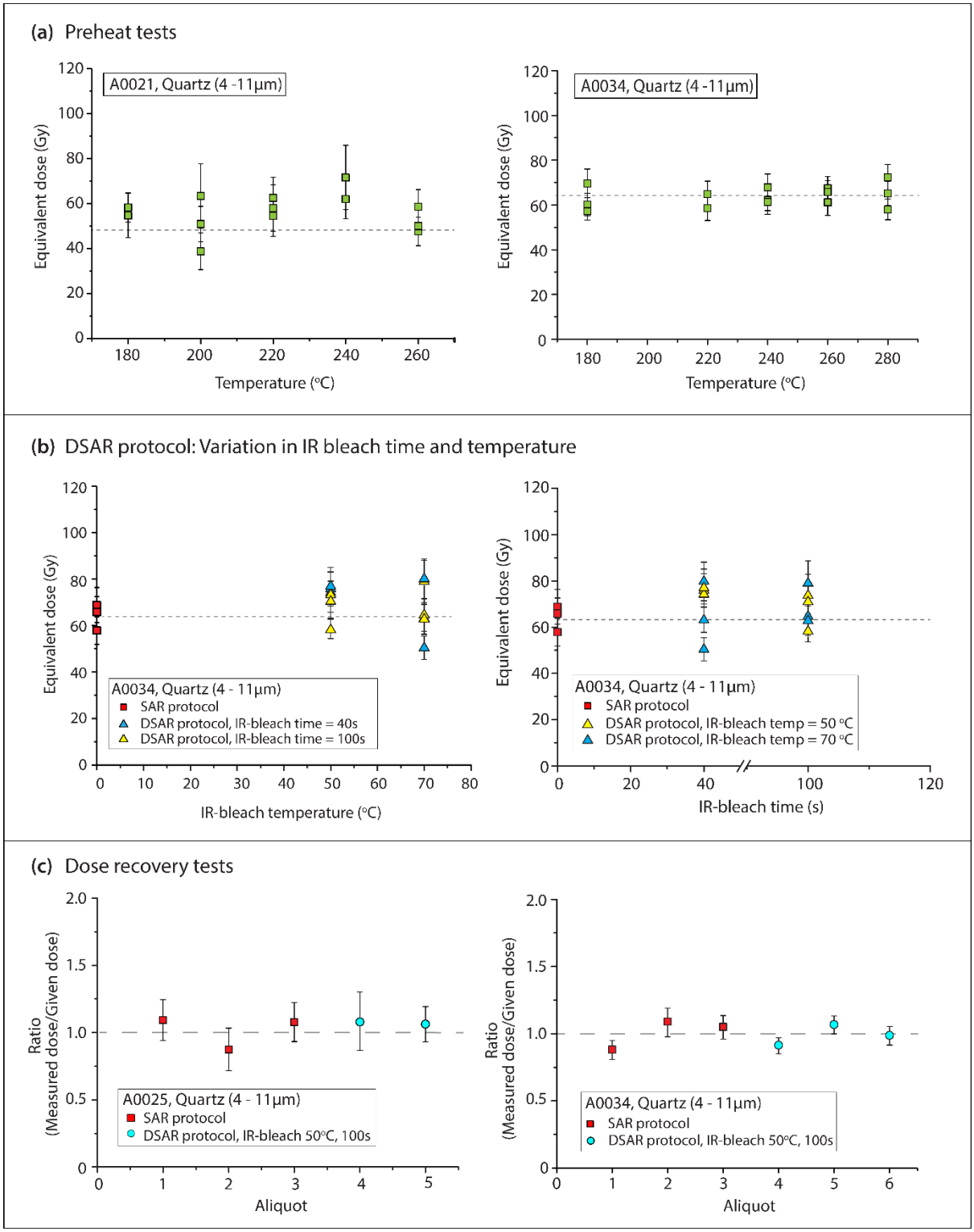

Fig. S3. (a) Dependence of equivalent dose (D_e) on preheat temperature during SAR protocols for selected samples A0021 (PAN) and A0034 (ASH) (b) Optimisation of the DSAR protocol: Variation in D_e with varying IR bleach temperature and IR bleach time respectively for sample A0034 (c) Dose recovery tests on selected samples (A0025 and A0034) using both SAR and DSAR protocols.

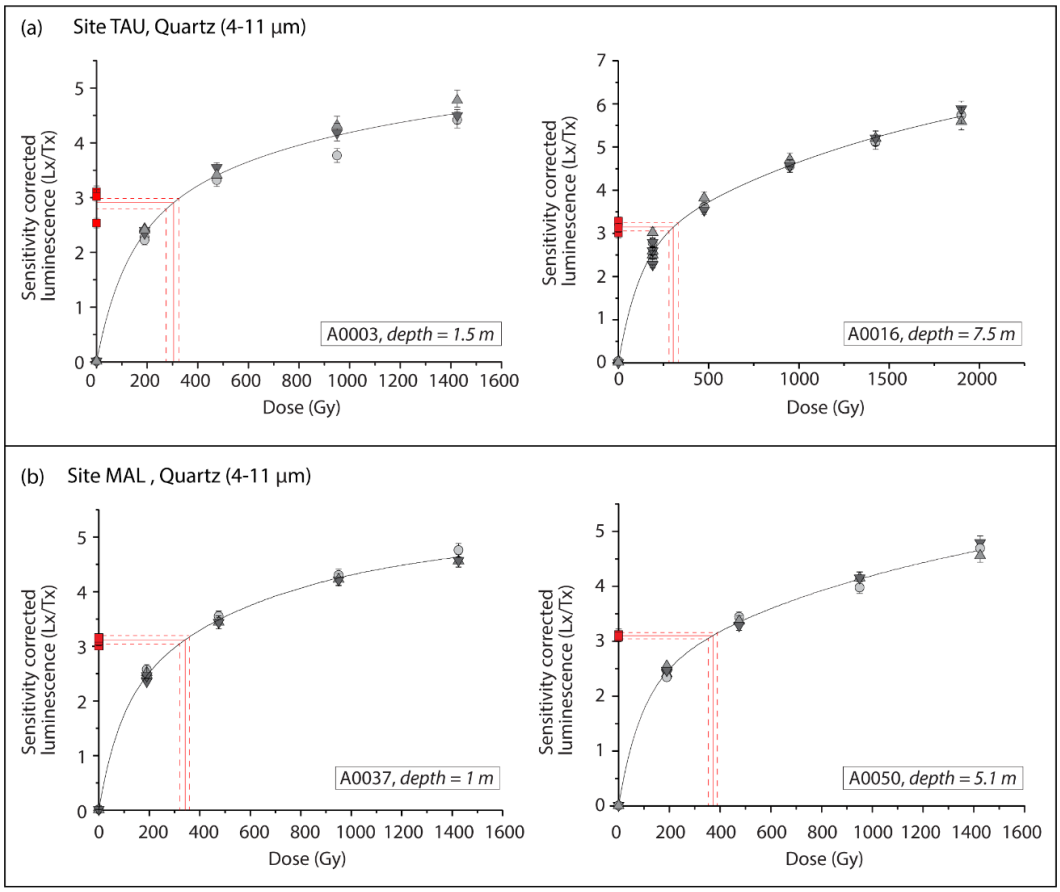

Fig. S4. Dose response curves (DRC) constructed at high doses (upto c.1500 Gy) in fine grain quartz from (a) site TAU and (b) site MAL. The DRCs were fitted using the sum of two saturating exponentials.

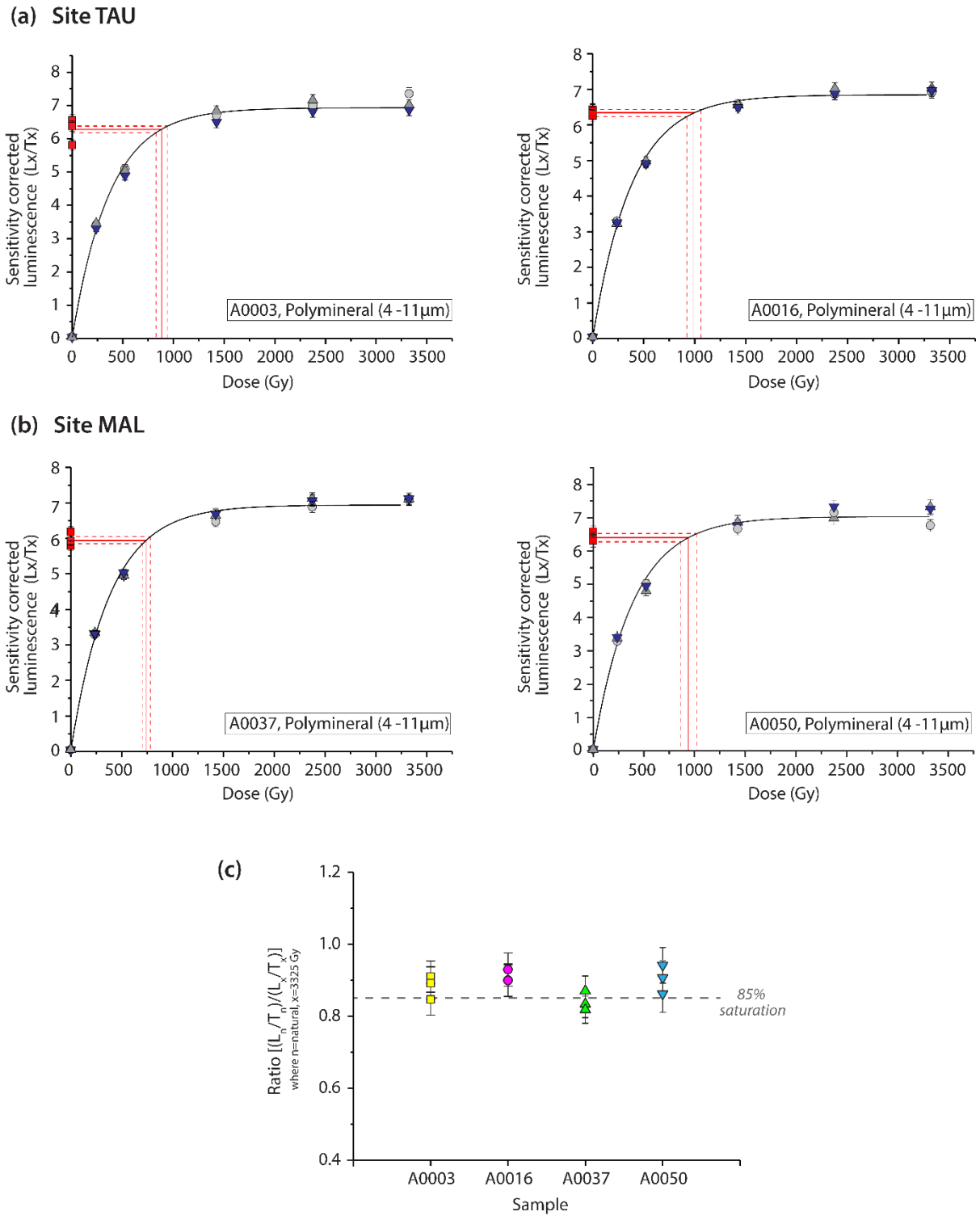

Fig. S5. Dose response curve for fine-grained polymineral samples at high doses (>3000 Gy) for selected samples from two sites: (a) site TAU, samples A0003 (depth 1.5 m) and A0016 (depth 7.5 m); and (b) site MAL, samples A0037 (depth 1 m) and A0050 (depth 5.1 m). (c) Ratio of natural sensitivity-corrected $pIRIR_{290}$ signal to that emitted at a dose of c. 3325 Gy for the aforementioned samples, taken from the top and bottom of the TAU and MAL sections.

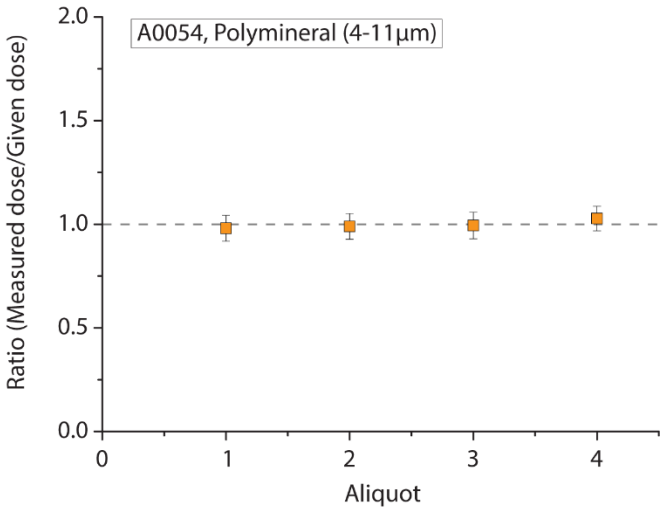

Fig. S6. Dose recovery tests for fine grained polymineral sample A0054 from site MAL.

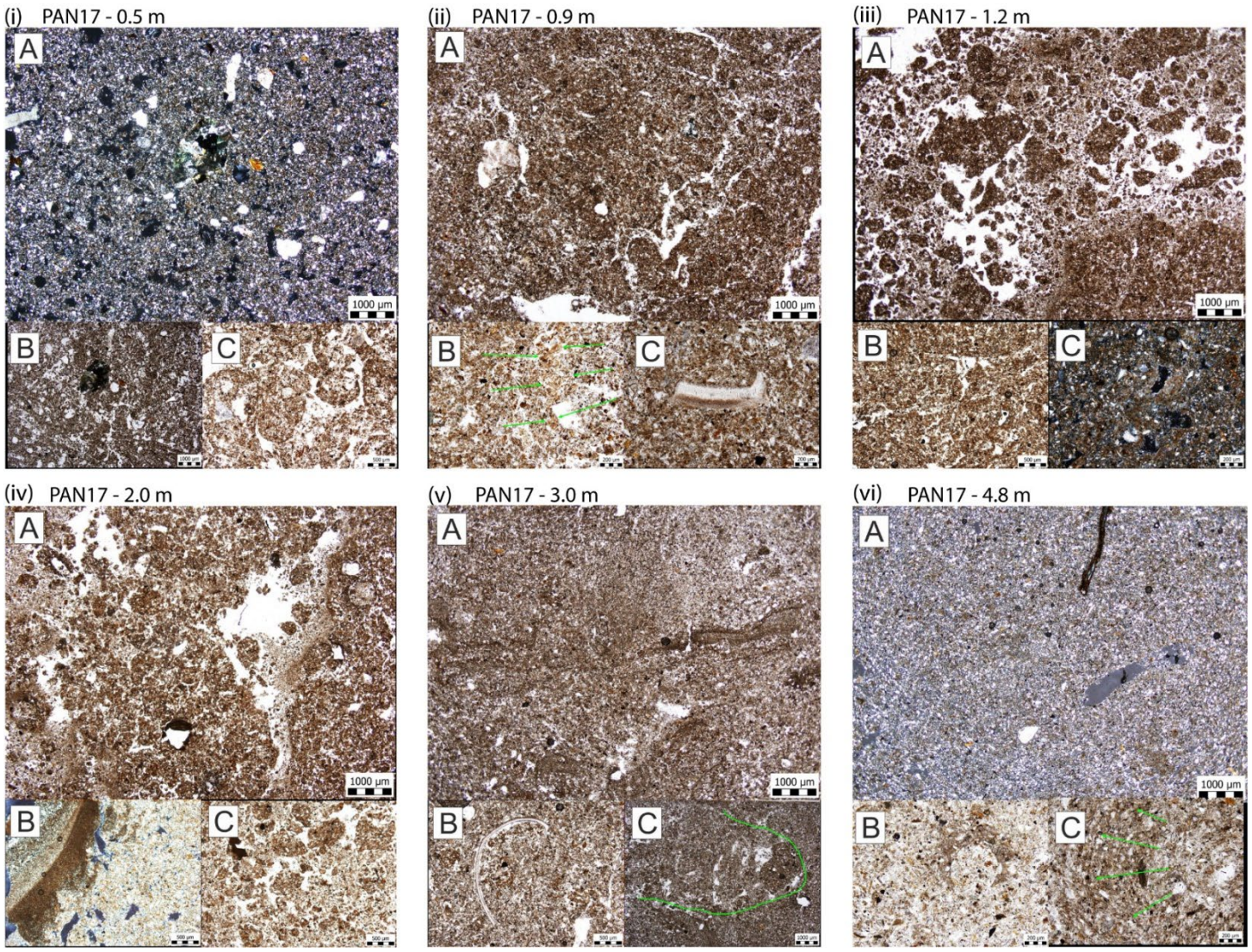

Fig. S7. Microphotographs of thin sections from profile PAN **(i)** PAN17-0.5 m: **A)** unsorted matrix (XPL). **B)** same photograph showing highly bioturbated matrix (PPL). **C)** excremental features (PPL).

(ii) PAN17-0.9 m: **A)** matrix with cracks, possibly a product of bioturbation (PPL**). B)** decomposed organic matter, probably root relict (PPL). **C)** shell fragment (PPL).

(iii) PAN17-1.2 m: **A)** Granular microstructure – problem in sampling? (PPL). **B)** passage features (PPL). **C)** vughs with hypocoating preserved within the aggregate (XPL).

(iv) PAN17-2.0 m: **A)** matrix rich in depletion features and redeposited soil crusts (PPL). **B)** Soil crust (XPL). **C)** silty aggregate fragments (PPL).

(v) PAN17-3.0 m: **A)** unsorted material with common presence of redeposited soil crusts (PPL). **B)** shell fragment (PPL). **C)** bioturbation (PPL).

(vi) PAN17-4.8 m: **A)** homogenous silty loam influenced by bioturbation (XPL). **B)** rare hypocoating (XPL). **C)** bioturbation (PPL).

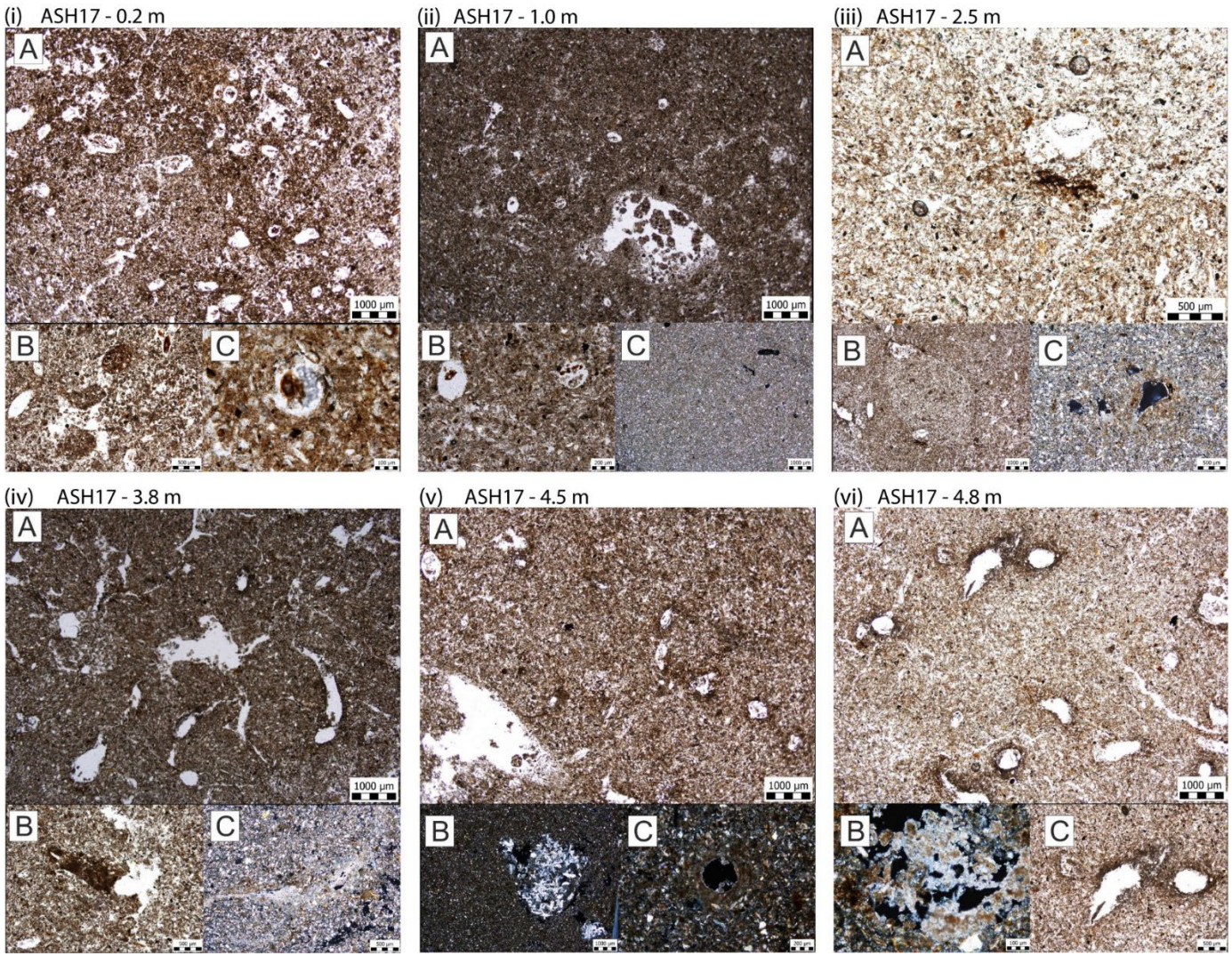

Fig. S8. Microphotographs of thin sections from profile ASH **(i)** ASH17-0.2 m: **A)** matrix influenced strongly by bioturbation (PPL). **B)** excremental features (PPL). **C)** multi-layered hypocoating with the root in the centre (PPL).

(ii) ASH17-1.0 m: **A)** homogenous silty loam influenced by bioturbation (PPL). **B)** Fresh roots preserved (PPL). **C)** homogeneous sorted matrix (XPL).

(iii) ASH17-2.5 m: **A)** dark brown concentrations of decomposed organic matter (PPL). **B)** calcium carbonate impregnations (XPL). **C)** hypocoating (XPL).

(iv) ASH17-3.8 m: **A)** homogeneous silty loam matrix with common bioturbation features (PPL). **B)** rare presence of soil crusts (PPL). **C)** calcium carbonate infill with possible presence of lublinite (XPL).

(v) ASH17-4.5 m: **A)** homogeneous silty loam matrix with common vughs and hypocoatings (PPL). **B)** gypsum crystals (XPL). **C)** calcium carbonate hypocoating (XPL).

(vi) ASH17-4.8 m: **A)** homogenous silty loam matrix with common vughs and hypocoatings (PPL). **B)** lublinite void infills (XPL). **C)** calcium carbonate hypocoating (XPL).

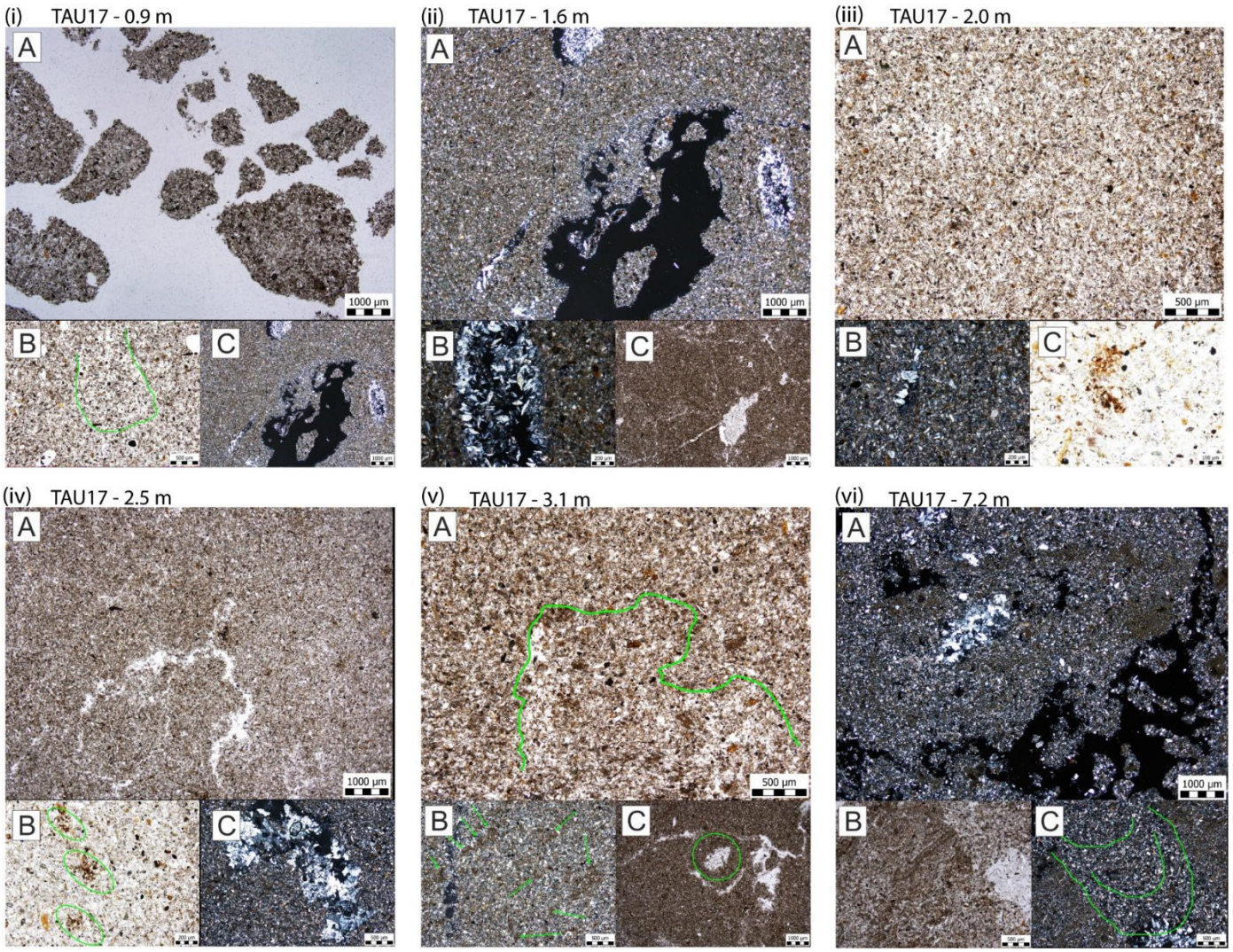

Fig. S9. Microphotographs of thin sections from site TAU **(i)** TAU17-0.9 m: **A)** granular microstructure – possibly a sampling error (PPL). **B)** passage features (PPL). **C)** vughs preserved within the aggregates and root fragments *(in green)* (PPL).

(ii) TAU17-1.6 m: **A)** homogeneous silty loam influenced by gypsum crystal growth (XPL). **B)** calcium carbonate impregnations (XPL). **C)** cracks as a result of crystal growth (PPL).

(iii) TAU17-2.0 m: **A)** homogeneous silty loam influenced by gypsum crystal growth (XPL). **B)** gypsum crystal growth (XPL). **C)** rare decomposed organic matter (PPL).

(iv) TAU17-2.5 m: **A)** homogenous silty loam matrix with cracks (XPL). **B)** decomposed organic matter (PPL). **C)** gypsum crystal growth (XPL).

(v) TAU17-3.1 m: **A)** homogeneous silty loam influenced by bioturbation (PPL). **B)** silty aggregates (XPL). **C)** subangular blocky microstructure and gypsum crystal growth *(green circle)* (PPL).

(vi) TAU17-7.2 m: **A)** packing voids through unsorted matrix rich in soil crust and gypsum crystal growth (XPL). **B)** soil crusts and gypsum crystal growth (PPL). **C)** bioturbation (XPL).

Table S1. Micromorphological description of selected samples from three loess sites (PAN, ASH and TAU) in the Ili basin, SE Kazakhstan.

Site	Micromorphological description of selected samples							
	Selected Sample (depth, m)	Fabric						Pedogenic features
		Microstructure	Matrix	Grain size description	Minerals	Roundness	Other features	
Panfilov (PAN)	0.5 m Fig. S7(i)	Complex microstructure (combination of granular and channel) with the simple packing, compound packing voids, channels and vughs.	Colour - Dark brown to brown; Bf - crystallitic	Unsorted with double spaced porphyric distribution; GSD corresponds to sandy loam with c/f$_{(50\mu m)}$= 60:40	Qzt, Ptg, aluminosilicate and opaque minerals	SR; some angular to sub-angular rock fragments	Decomposed organic matter, relicts of fresh roots	Passage and excremental features
	0.9 m Fig. S7(ii)	Complex microstructure with the cracks, vughs and channels.	Colour - brown; Bf- crystallitic	Moderately sorted with porphyric distribution; GSD corresponds to silty loam with c/f$_{(50\mu m)}$= 40:60	Qzt, Ptg, aluminosilicate and opaque minerals	SR; some angular rock fragments	Decomposed organic matter, relicts of fresh roots, presence of shell fragments	Passage features, hypocoatings
	1.2 m Fig. S7(iii)	Presence of granular microstructure (problematic sampling issue?). Preserved pores most likely reflect the complex packing void; few vughs preserved within aggregates.	Colour - grey brown; Bf- crystallitic	Well sorted with porphyric distribution; GSD corresponds to silty loam with c/f$_{(50\mu m)}$= 30:70	Qzt, Ptg, aluminosilicate and opaque minerals	SR	Decomposed organic matter	Rare passage features, hypocoatings
	2.0 m Fig. S7(iv)	Complex microstructure with complex packing voids and chambers; few vughs and channels are also preserved.	Colour - grey brown to brown, Bf - crystallitic	Moderately sorted to unsorted with double spaced porphyric distribution; GSD corresponds to silty loam with c/f$_{(50\mu m)}$= 40:60	Qzt, Ptg, aluminosilicate and opaque minerals	SR	Decomposed organic matter	Passage features, depletion features, calcium carbonate impregnations, redeposited soil crusts

	3.0 m Fig. S7(v)	Complex microstructure with the complex packing void, few vughs and cracks	Colour - Patchy brown and dark brown phases; Bf-crystallitic	Unsorted with the porphyric double spaced distribution; GSD corresponds to the sandy loam withc/$f_{(50\mu m)}$=60:40; presence of silty aggregates (compose 10% of sandy fraction)	Qzt, Ptg, aluminosilicate and opaque minerals	SR	Decomposed organic matter	Passage features, calcium carbonate impregnations, fragmented and redeposited soil crusts
	4.8 m Fig. S7(vi)	Complex microstructure with the few vughs, chambers and and channels, with a low amount of pores.	Colour - grey brown; Bf-crystallitic	Well sorted with the porphyric distribution and GSD corresponds to the silty loam withc/f $_{(50\mu m)}$= 60:40;presence of silty aggregates (compose 10% of sandy fraction)	Qzt, Ptg, aluminosilicate and opaque minerals	SR	Decomposed organic matter	Rare passage features
Ashubulak (ASH)	0.2 m Fig. S8(i)	Complex microstructure (combination of granular and channel) simple packing voids, compound packing voilds, channels and few vughs.	Colour - dark brown; Bf-crystallitic	Well sorted with porphyric distribution; GSD correspond to silty loam with c/$f_{(50\mu m)}$= 30:70.	Qzt, Ptg, aluminosilicate and opaque minerals	SR	Decomposed organic matter	Passage features, excremental features, partial and multilayered hypocoating.
	1.0 m Fig. S8(ii)	Complex microstructure with the complex packing void, few cracks, vughs and channels	Colour - grey brown; Bf-crystallitic	Well sorted with porphyric distribution and GSD corresponds to the silty loam with c/$f_{(50\mu m)}$= 30:70	Qzt, Ptg, aluminosilicate and opaque minerals	SR	Decomposed organic matter	Passage features
	2.5m Fig. S8(iii)	Channel microstructure with channels, vughs and chambers	Colour- brown with local dark brown	Moderately sorted with porphyric distribution and GSD corresponds to silty	Qzt, Ptg, aluminosilicate and opaque minerals	SR	Decomposed organic matter as black dotting	Passage features, calcium carbonate illuviation, hypocoating

			patches; Bf-crystallic	loam with c/$f_{(50\mu m)}$= 30:70				
	3.8 m Fig. S8(iv)	Complex microstructure with the complex packing void, cracks, vughs and channels. Pores are very common	Colour - grey brown; Bf-crystallitic	Well sorted with porphyric distribution; GSD corresponds to the silty loam with the c/$f_{(50\mu m)}$= 30:70	Qzt, Ptg, aluminosilicate and opaque minerals	SR	Decomposed organic matter, relicts of fresh roots, rare presence of soil crusts	Passage features, hypocoating, infilling
	4.5 m Fig. S8(v)	vughy/channel microstructure with the vughs and channels.	Colour - grey brown; Bf-crystallitic	Well sorted with the porphyric distribution; GSD corresponds to the silty loam with c/$f_{(50\mu m)}$= 30:70	Qzt, Ptg, aluminosilicate and opaque minerals	SR	Decomposed organic matter, relicts of fresh roots	Rare passage features, hypocoating, gypsum crystal growth
	4.8 m Fig. S8(vi)	Channel microstructure with the vughs and channels.	Colour - grey brown; Bf-crystallitic	Well sorted with the porphyric distribution; GSD corresponds to the silty loam with c/$f_{(50\mu m)}$= 30:70	Qzt, Ptg, aluminosilicate and opaque minerals	SR	Decomposed organic matter, occasional relicts of fresh roots	Rare passage features, hypocoating, lignite void infillings, gypsum crystal growth
Taukaraturyuk (TAU)	0.9 m Fig. S9(i)	Granular microstructure (product of problematic sampling?). Preserved pores may be because of the complex packing void; few vughs preserved within the aggregates.	Colour - grey brown; Bf-crystallitic	Well sorted with the porphyric distribution; GSD corresponds to the silty loam with c/$f_{(50\mu m)}$= 30:70	Qzt, Ptg, aluminosilicate and opaque minerals	SR	Decomposed organic matter	Rare passage features
	1.6 m Fig. S9(ii)	Complex microstructure with the chambers and cracks.	Colour - grey brown; Bf - crystallitic	Well sorted with porphyric distribution and GSD corresponds to silty loam with with c/$f_{(50\mu m)}$= 30:70	Qzt, Ptg, aluminosilicate and opaque minerals, gypsum	SR, except gypsum crystals	Decomposed organic matter	Gypsum crystallisation

	2.0 m Fig. S9(iii)	Massive microstructure with only rare vughs	Colour - grey brown; Bf - crystallitic	Well sorted with the porphyric distribution and GSD corresponds to the silty loam with $c/f_{(50\mu m)}$= 30:70.	Qzt, Ptg, alumosilicate and opaque minerals, gypsum	SR, except gypsum crystals	Decomposed organic matter	Gypsum crystallisation
	2.5 m Fig. S9(iv)	Massive to cracky microstructure with only rare vughs	Colour - grey brown; Bf - crystallitic	Well sorted with the porphyric distribution and GSD corresponds to the silty loam with $c/f_{(50\mu m)}$= 30:70.	Qzt, Ptg, alumosilicate and opaque minerals, gypsum	SR, except gypsum crystals	Decomposed organic matter as black dotting, brownish organic matter	Occasional gypsum crystallisation
	3.1 m Fig. S9(v)	Subangular blocky microstructure with the complex packing void, few vughs and channels.	Colour - grey brown; Bf - crystallitic	Well sorted with porphyric distribution and GSD correspond to the silty loam with $c/f_{(50\mu m)}$= 60:40; presence of silty aggregates (compose up to 10 % of the sandy fraction)	Qzt, Ptg, alumosilicate and opaque minerals, gypsum	SR, except gypsum crystals	Decomposed organic matter	Rare passage features and gypsum crystal growth
	7.2 m Fig. S9(vi)	Subangular blocky microstructure with the complex packing void, chambers, plates as a part of fragmented soil crusts, few vughs and channels	Colour - Patchy brown and dark brown phases; Bf - crystallitic	Unsorted with porphyric double spaced distribution and GSD correspond to the sandy loam with the $c/f_{(50\mu m)}$= 60:40; coarse fraction mainly composed of soil fragments, gypsum crystals and rock fragments	Qzt, Ptg, alumosilicate and opaque minerals, gypsum, rock fragments	SR, except gypsum crystals	Decomposed organic matter	Passage features, calcium carbonate illuviation and local impregnations, fragmented and redeposited soil crust, gypsum crystal growth

*Terms: *Qzt* – quartz; *SR* – subrounded; *Bf* - Bifringence; *Ptg* - ; *GSD* - Grain size distribution

Table S2. Equivalent dose, dose rate and post $IR_{50}IRSL_{290}$ ages on polymineral fine grains from the Ili basin study sites. The term n_e/n_t refers to the total number of accepted discs to the total number of discs measured

Site	Sample No.	Depth (m)	Moisture attenuated dose rate (Gy/ka)			Cosmic (Gy/ka)	Total Dose Rate (Gy/ka)	n_e/n_t	D_e (Gy)	Age (ka)
			Alpha	Beta	Gamma					
Taukaraturyuk (TAU)	A003	1.5 ± 0.05	1.1 ± 0.1	2.0 ± 0.1	1.2 ± 0.1	0.20 ± 0.02	4.5 ± 0.2	8/12	896.6 ± 54.0	197.6 ± 21.2
	A007	3.5 ± 0.05	1.3 ± 0.1	2.2 ± 0.2	1.3 ± 0.1	0.15 ± 0.02	5.1 ± 0.3	5/5	953.5 ± 65.7	188.7 ± 22.8
	A0012	6.0 ± 0.05	1.3 ± 0.1	2.3 ± 0.2	1.4 ± 0.1	0.11 ± 0.01	5.1 ± 0.2	5/5	1004.4 ± 66.9	197.3 ± 22.3
	A0016	7.5 ± 0.05	1.2 ± 0.1	2.3 ± 0.2	1.3 ± 0.1	0.10 ± 0.01	4.9 ± 0.2	5/5	1017.9 ± 63.5	207.7 ± 22.3
Malubai (MAL)	*A0037**	*1.0 ± 0.05*	*1.3 ± 0.2*	*2.0 ± 0.2*	*1.2 ± 0.1*	*0.21 ± 0.02*	*4.7 ± 0.2*	*4/4*	*959.0 ± 55.8*	*204.9 ± 22.8*
	A0037[#]	1.0 ± 0.05	–	–	–	–	6.0 ± 0.3	4/4	959.0 ± 55.8	158.5 ± 17.0
	A0038	1.5 ± 0.05	1.8 ± 0.2	2.5 ± 0.2	1.6 ± 0.1	0.20 ± 0.02	6.0 ± 0.3	3/3	1031.5 ± 83.6	170.5 ± 22.2
	A0040	2.4 ± 0.05	1.6 ± 0.2	2.5 ± 0.2	1.5 ± 0.1	0.18 ± 0.02	5.7 ± 0.3	4/5	1111.1 ± 98.6	195.0 ± 27.0
	A0050	5.1 ± 0.05	1.6 ± 0.2	2.5 ± 0.2	1.6 ± 0.1	0.13 ± 0.01	5.8 ± 0.3	4/5	1040.1 ± 91.0	179.3 ± 25.0

*Sample A0037 originally (in *italics*) has an unusually low Uranium content (See supplementary Table S4) compared to the rest of the section.
[#]We use the dose rate of the sample below A0037 (here A0038) to evaluate the more likely apparent age of the sample.

Table S3. (a) DSAR and (b) SAR protocol used in the study for D_e determinations of fine-grained quartz grains (c) $pIR_{50}IR_{290}$ protocol used for the measurement of polymineral fine grains.

(a) Double-SAR protocol (Modified from Banerjee et al, 2001)		
Step	Treatment	Signal measured
1	Dose (Natural or laboratory)	-
2	Preheat 10s at 260 ^oC	
3	IR, 100s at 50^oC	
4	Blue OSL, 40s at 125 ^oC	L_n, or L_x
5	Test dose	
6	Cut heat 10s at 240 ^oC	
7	IR, 100s at 50^oC	
8	Blue OSL, 40s at 125 ^oC	T_n or T_x
9	Blue OSL, 40s 280 ^oC	
10	Return to step 1	

(b) SAR protocol (Murray and Wintle, 2000)		
Step	Treatment	Signal measured
1	Dose (Natural or laboratory)	-
2	Preheat 10s at 260 ^oC	
3	Blue OSL, 40s at 125 ^oC	L_n, or L_x
4	Test dose	
5	Cut heat 10s at 240 ^oC	
6	Blue OSL, 40s at 125 ^oC	T_n or T_x
7	Blue OSL, 40s 280 ^oC	
8	Return to step 1	

(c) $pIR_{50}IR_{290}$ protocol (after Thiel et al, 2011)		
Step	Treatment	Signal measured
1	Dose (Natural or laboratory)	-
2	Preheat 60s at 320 ^oC	
3	IRSL, 200s at 50^oC	
4	IRSL, 200s at 290 ^oC	L_n or L_x
5	Test dose	
6	Preheat 60s at 320 ^oC	
7	IRSL, 200s at 50^oC	T_n or T_x
8	IRSL, 200s at 290 ^oC	
9	IRSL, 100s at 325 ^oC	
10	Return to step 1	

Table S4. Radionuclide activities ($Bq.kg^{-1}$) and daughter to parent ratios obtained from high resolution gamma spectrometry measurements of the ^{238}U and ^{232}Th decay chains.

Sample No.	Depth (m)	^{238}U-Chain ($Bq.kg^{-1}$)			^{232}Th Chain ($Bq.kg^{-1}$)			Ratios - U chain		Ratios - Th	
		^{238}U	^{226}Ra	^{210}Pb	^{232}Th	^{228}Ra	^{228}Th	$^{226}Ra/^{238}U$	$^{210}Pb/^{226}Ra$	$^{228}Ra/^{232}Th$	$^{228}Th/^{228}Ra$
A0017	1	35 ± 5	43.5 ± 2.6	35 ± 4	47.1 ± 2.9	48 ± 3	46.6 ± 2.9	1.24	0.80	1.02	0.97
A0019	2	34 ± 4	36.9 ± 2.3	32 ± 4	42.4 ± 2.5	40 ± 3	43 ± 2.8	1.09	0.87	0.94	1.08
A0021	3	40 ± 5	39.5 ± 2.3	31 ± 4	44.2 ± 2.7	45 ± 3	44 ± 2.8	0.99	0.78	1.02	0.98
A0023	4	41 ± 5	39.7 ± 2.5	32 ± 4	43.2 ± 2.8	43 ± 3	43.3 ± 2.8	0.97	0.81	1.00	1.01
A0025	5	38 ± 5	39.5 ± 2.4	37 ± 5	47 ± 3	47 ± 3	47 ± 3	1.04	0.94	1.00	1.00
A0026	0.5	29 ± 5	36.5 ± 2.2	28 ± 4	40.7 ± 2.6	42 ± 2.8	40.3 ± 2.6	1.26	0.77	1.03	0.96
A0028	1.5	46 ± 5	40.5 ± 2.5	38 ± 5	44.2 ± 2.8	43 ± 3	44.6 ± 2.9	0.88	0.94	0.97	1.04
A0030	2.5	43 ± 6	40.3 ± 2.5	32 ± 4	45.2 ± 2.9	45 ± 3	45.2 ± 2.9	0.94	0.79	1.00	1.00
A0032	3.5	38 ± 5	42.3 ± 2.5	39 ± 4	48 ± 3	47 ± 3	49 ± 3	1.11	0.92	0.98	1.04
A0034	4.5	40 ± 5	40.9 ± 2.5	33 ± 4	46 ± 3	46 ± 3	46 ± 3	1.02	0.81	1.00	1.00
A001	0.5	29 ± 4	36.4 ± 2.3	30 ± 4	41.3 ± 2.6	42 ± 3	41 ± 2.7	1.26	0.82	1.02	0.98
A002	1	37 ± 5	44.2 ± 2.6	41 ± 5	47 ± 2.9	48 ± 3	46.7 ± 2.9	1.19	0.93	1.02	0.97
A003	1.5	46 ± 5	40.5 ± 2.4	36 ± 4	39.5 ± 2.5	39.1 ± 2.7	39.6 ± 2.5	0.88	0.89	0.99	1.01
A007	3.5	56 ± 5	50 ± 2.8	43 ± 4	42.8 ± 2.6	43 ± 3	43 ± 3	0.89	0.86	1.00	1.00
A0012	6	54 ± 5	48.1 ± 2.8	43 ± 4	45.3 ± 2.8	46 ± 3	45.2 ± 2.8	0.89	0.89	1.02	0.98
A0016	7.5	44 ± 4	41.2 ± 2.3	36 ± 3	47.4 ± 2.9	48 ± 3	47.3 ± 2.9	0.94	0.87	1.01	0.99
A0037	1	59 ± 6	58 ± 3	47 ± 5	36.5 ± 2.3	36.4 ± 2.5	36.5 ± 2.3	0.98	0.81	1.00	1.00
A0038	1.5	97 ± 8	60 ± 3	42 ± 5	38.4 ± 2.4	39 ± 2.6	38.3 ± 2.4	0.62	0.70	1.02	0.98
A0040	2.4	71 ± 8	62 ± 4	53 ± 6	45.6 ± 2.9	46 ± 3	45.6 ± 2.9	0.87	0.85	1.01	0.99
A0050	5.1	75 ± 8	60 ± 4	42 ± 5	48 ± 3	47 ± 3	48 ± 3	0.80	0.70	0.98	1.02

Table S5. List of sites from the ACA and CLP considered for age depth modelling and consequently for evaluation of MARs. The references in the table refer to the studies from which the luminescence ages for the sites have been obtained.

Site	Site names	Reference
Sites from the Ili basin, ACA		
MBK	Maibulak	Fitzsimmons et al (2017)
REM	Remizovka	This study; Fitzsimmons et al (2018)
PAN	Panfilov	This study
ASH	Ashubulak	This study
XEBLK	Xiaoerbulak	Li et al (2016)a
TLD	Talede	Kang et al (2015)
TLD16	Talede	Wang et al (2019)a
NLK	Nilka	Song et al (2015)
ZKT	Zeketai	E et al (2012)
KS15	Kunes-15	Li et al (2018)
KS15-05	Kunes15-05	Wang et al (2019)b
ZSP	Zhaoso Puma	Song et al (2012)
NLT17	Nalatizhen 17	Li et al (2020)
XY17	Xinyuan 17	Li et al (2020)
Sites from basins neighboring the Ili basin, ACA		
VAL	Valikhanova	Fitzsimmons et al (2017)
BSK	Bishkek	Youn et al (2014)
BYH10	--	Li et al (2016)b
LJW10	Lujiaowan	Li et al (2015)
SCZ17	Shichengzi	Duan et al (2020)
YM	Yumin	Li et al (2019)
TC	Tacheng	Li et al (2019)
QS16	Qingshui	Li et al (2020)
Sites from the Chinese loess Plateau		
GL	Gulang	Sun et al (2012)
JY	Jinguan	Sun et al (2012)
XF	Xifeng	Stevens et al (2016)
BGY	Beiguoyuan	Stevens et al (2008)
YB	Yuanbao	Lai and Wintle (2006)
TXD	Tuxiangdao	Buylaert et al (2008)
WN	Weinan	Kang et al (2013)
XY	Xunyi	Stevens et al (2008)
ZJC	Zhongjiacai	Buylaert et al (2008)
LC	Luochuan	Lu et al (2007)
MN	Mangshan	Qui and Zhou (2015)

References:

Avram, A., Constantin, D., Veres, D., Kelemen, S., Obreht, I., Hambach, U., Marković, S. B., & Timar-Gabor, A. (2020). Testing polymineral post-IR IRSL and quartz SAR-OSL protocols on Middle to Late Pleistocene loess at Batajnica, Serbia. *Boreas*, *49*(3), 615–633. https://doi.org/10.1111/bor.12442

Banerjee, D., Murray, A. S., Bøtter-Jensen, L., & Lang, A. (2001). Equivalent dose estimation using a single aliquot of polymineral fine grains. *Radiation Measurements*, *33*(1), 73–94. doi: 10.1016/S1350-4487(00)00101-3

Blaauw, M., & Christen, J. A. (2011). Flexible paleoclimate age-depth models using an autoregressive gamma process. *Bayesian Analysis*, *6*(3), 457–474. https://doi.org/10.1214/11-BA618

Buylaert, J. P., Murray, A. S., Vandenberghe, D., Vriend, M., Corte, F. D., & haute, P. V. den. (2008). Optical dating of Chinese loess using sand-sized quartz: Establishing a time frame for Late Pleistocene climate changes in the western part of the Chinese Loess Plateau. *Quaternary Geochronology*, *3*(1), 99–113. doi: https://doi.org/10.1016/j.quageo.2007.05.003

Buylaert, J.-P., Jain, M., Murray, A. S., Thomsen, K. J., Thiel, C., & Sohbati, R. (2012). A robust feldspar luminescence dating method for Middle and Late Pleistocene sediments. *Boreas*, *41*(3), 435–451. doi: https://doi.org/10.1111/j.1502-3885.2012.00248.x

Buylaert, J.-P., Yeo, E.-Y., Thiel, C., Yi, S., Stevens, T., Thompson, W., Frechen, M., Murray, A., & Lu, H. (2015). A detailed post-IR IRSL chronology for the last interglacial soil at the Jingbian loess site (northern China). *Quaternary Geochronology*, 194–199. https://doi.org/10.1016/j.quageo.2015.02.022

Cunningham, A. C., & Wallinga, J. (2010). Selection of integration time intervals for quartz OSL decay curves. *Quaternary Geochronology*, *5*(6), 657–666. doi: 10.1016/j.quageo.2010.08.004

Duan, F., An, C., Wang, W., Herzschuh, U., Zhang, M., Zhang, H., Liu, Y., Zhao, Y., & Li, G. (2020). Dating of a late Quaternary loess section from the northern slope of the Tianshan Mountains (Xinjiang, China) and its paleoenvironmental significance. *Quaternary International*, *544*, 104–112. https://doi.org/10.1016/j.quaint.2020.02.034

Duller, G. A. T. (2003). Distinguishing quartz and feldspar in single grain luminescence measurements. *Radiation Measurements*, *37*(2), 161–165. https://doi.org/10.1016/S1350-4487(02)00170-1

Durcan, J. A., King, G. E., & Duller, G. A. T. (2015). DRAC: Dose Rate and Age Calculator for trapped charge dating. *Quaternary Geochronology*, *28*, 54–61. doi: 10.1016/j.quageo.2015.03.012

E. ChongYi, Lai, Z., Sun, Y., Hou, G., Yu, L., & Wu, C. (2012). A luminescence dating study of loess deposits from the Yili River basin in western China. *Quaternary Geochronology*, *10*, 50–55. doi: https://doi.org/10.1016/j.quageo.2012.04.022

Fitzsimmons, K. E., Iovita, R., Sprafke, T., Glantz, M., Talamo, S., Horton, K., … Taimagambetov, Z. (2017). A chronological framework connecting the early Upper Palaeolithic across the Central Asian piedmont. *Journal of Human Evolution*, *113*, 107–126. doi: https://doi.org/10.1016/j.jhevol.2017.07.006

Fitzsimmons, K. E., Sprafke, T., Zielhofer, C., Günter, C., Deom, J.-M., Sala, R., & Iovita, R. (2018). Loess accumulation in the Tian Shan piedmont: Implications for palaeoenvironmental change in arid Central Asia. *Aeolian Deposition and Earth Surface Systems*, *469*, 30–43. doi: 10.1016/j.quaint.2016.07.041

Frechen, M., Schweitzer, U., & Zander, A. (1996). Improvements in sample preparation for the fine grain technique. *Ancient TL*, *14*(2), 15–17.

Galbraith, R. F., Roberts, R. G., Laslett, G. M., Yoshida, H., & Olley, J. M. (1999). Optical dating of single and multiple grains of quartz from Jinmium rock shelter, northern Australia: Part I, experimental design and statistical models. *Archaeometry*, *41*(2), 339–364. Scopus. doi: 10.1111/j.1475-4754.1999.tb00987.x

Guérin, G., Mercier, N., & Adamiec, G. (2011). Dose-rate conversion factors: Update. *Ancient TL*, *29*(1), 5–8.

Jackson, M. L., Sayin, M., & Clayton, R. N. (1976). Hexafluorosilicic Acid Reagent Modification for Quartz Isolation. *Soil Science Society of America Journal*, *40*(6), 958–960. doi: 10.2136/sssaj1976.03615995004000060040x

Jain, M., & Singhvi, Ashok. K. (2001). Limits to depletion of blue-green light stimulated luminescence in feldspars: Implications for quartz dating. *Radiation Measurements*, *33*(6), 883–892. doi: 10.1016/S1350-4487(01)00104-4

Kang, S., Wang, X., & Lu, Y. (2013). Quartz OSL chronology and dust accumulation rate changes since the Last Glacial at Weinan on the southeastern Chinese Loess Plateau: Quartz OSL chronology and dust accumulation rates, SE Chinese Loess Plateau. *Boreas*, 815-829. doi: 10.1111/bor.12005

Kang, S., Wang, X., Lu, Y., Liu, W., Song, Y., & Wang, N. (2015). A high-resolution quartz OSL chronology of the Talede loess over the past ∼30 ka and its implications for dust accumulation in the Ili Basin, Central Asia. *Quaternary Geochronology*, *30*, 181–187. doi: 10.1016/j.quageo.2015.04.006

Jia, J., Liu, H., Gao, F., & Xia, D. (2018). Variations in the westerlies in Central Asia since 16 ka recorded by a loess section from the Tien Shan Mountains. *Palaeogeography, Palaeoclimatology, Palaeoecology*, *504*, 156–161. https://doi.org/10.1016/j.palaeo.2018.05.021

Kohfeld, K. E., & Harrison, S. P. (2003). Glacial-interglacial changes in dust deposition on the Chinese Loess Plateau. *Quaternary Science Reviews*, *22*(18), 1859–1878. https://doi.org/10.1016/S0277-3791(03)00166-5

Lai, Z.-P., & Wintle, A. G. (2006). Locating the boundary between the Pleistocene and the Holocene in Chinese loess using luminescence. *The Holocene*, *16*(6), 893–899. doi: 10.1191/0959683606hol980rr

Li, G., Wen, L., Xia, D., Duan, Y., Rao, Z., Madsen, D. B., Wei, H., Li, F., Jia, J., & Chen, F. (2015). Quartz OSL and K-feldspar pIRIR dating of a loess/paleosol sequence from arid central Asia, Tianshan Mountains, NW China. *Quaternary Geochronology*, *28*, 40–53. Scopus. https://doi.org/10.1016/j.quageo.2015.03.011

Li, Y., Song, Y., Lai, Z., Han, L., & An, Z. (2016)a. Rapid and cyclic dust accumulation during MIS 2 in Central Asia inferred from loess OSL dating and grain-size analysis. *Scientific Reports*, *6*(1), 32365. doi: 10.1038/srep32365

Li, G., Rao, Z., Duan, Y., Xia, D., Wang, L., Madsen, D. B., Jia, J., Wei, H., Qiang, M., Chen, J., & Chen, F. (2016)b. Paleoenvironmental changes recorded in a luminescence dated loess/paleosol sequence from the Tianshan Mountains, arid central Asia, since the Penultimate Glaciation. *Earth and Planetary Science Letters*, *448*, 1–12. https://doi.org/10.1016/j.epsl.2016.05.008

Li, G., Chen, F., Xia, D., Yang, H., Zhang, X., Madsen, D., Oldknow, C., Wei, H., Rao, Z., & Qiang, M. (2018). A Tianshan Mountains loess-paleosol sequence indicates anti-phase climatic variations in arid central Asia and in East Asia. *Earth and Planetary Science Letters*, *494*, 153–163. https://doi.org/10.1016/j.epsl.2018.04.052

Li, Y., Song, Y., Yin, Q., Han, L., & Wang, Y. (2019). Orbital and millennial northern mid-latitude westerlies over the last glacial period. *Climate Dynamics*, *53*(5–6), 3315–3324. doi: 10.1007/s00382-019-04704-5

Li, G., Yang, H., Stevens, T., Zhang, X., Zhang, H., Wei, H., Zheng, W., Li, L., Liu, X., Chen, J., Xia, D., Oldknow, C., Ye, W., & Chen, F. (2020). Differential ice volume and orbital modulation of Quaternary moisture patterns between Central and East Asia. *Earth and Planetary Science Letters*, *530*, 115901. https://doi.org/10.1016/j.epsl.2019.115901

Lu, Y. C., Wang, X. L., & Wintle, A. G. (2007). A new OSL chronology for dust accumulation in the last 130,000 yr for the Chinese Loess Plateau. *Quaternary Research*, *67*(1), 152–160. doi: 10.1016/j.yqres.2006.08.003

Murray, A. S., & Wintle, A. G. (2000). Luminescence dating of quartz using an improved single-aliquot regenerative-dose protocol. *Radiation Measurements*, *32*(1), 57–73. https://doi.org/10.1016/S1350-4487(99)00253-X

Murray, A. S., & Wintle, A. G. (2003). The single aliquot regenerative dose protocol: Potential for improvements in reliability. *Radiation Measurements*, *37*(4), 377–381. https://doi.org/10.1016/S1350-4487(03)00053-2

Murray, A. S., Buylaert, J. P., Thomsen, K. J., & Jain, M. (2009). The effect of preheating on the IRSL signal from feldspar. *Radiation Measurements*, *44*(5), 554–559. https://doi.org/10.1016/j.radmeas.2009.02.004

Olley, J. M., Murray, A., & Roberts, R. G. (1996). The effects of disequilibria in the uranium and thorium decay chains on burial dose rates in fluvial sediments. *Quaternary Science Reviews*, *15*(7), 751–760. doi: 10.1016/0277-3791(96)00026-1

Prescott, J. R., & Hutton, J. T. (1994). Cosmic ray contributions to dose rates for luminescence and ESR dating: Large depths and long-term time variations. *Radiation Measurements*, *23*(2), 497–500. doi: 10.1016/1350-4487(94)90086-8

Qiu, F., & Zhou, L. (2015). A new luminescence chronology for the Mangshan loess-palaeosol sequence on the southern bank of the Yellow River in Henan, central China. *Quaternary Geochronology*, *30*, 24–33. doi: 10.1016/j.quageo.2015.06.014

Rees-Jones, J. (1995). Optical dating of young sediments using fine-grained quartz. *Ancient TL*, *13*, 9–14.

Roberts, H. M., & Wintle, A. G. (2001). Equivalent dose determinations for polymineralic fine-grains using the SAR protocol: Application to a Holocene sequence of the Chinese Loess Plateau. *Quaternary Science Reviews*, *20*(5), 859–863. doi: 10.1016/S0277-3791(00)00051-2

Song, YouGui, Lai, Z., Li, Y., Chen, T., & Wang, Y. (2015). Comparison between luminescence and radiocarbon dating of late Quaternary loess from the Ili Basin in Central Asia. *Quaternary Geochronology*, *30*, 405–410. doi: 10.1016/j.quageo.2015.01.012

Song, Yougui, Li, C., Zhao, J., Cheng, P., & Zeng, M. (2012). A combined luminescence and radiocarbon dating study of the Ili loess, Central Asia. *13th International Conference on Luminescence and Electron Spin Resonance Dating - LED 2011 Dedicated to J. Prescott and G. Berger*, *10*, 2–7. doi: 10.1016/j.quageo.2012.04.005

Stevens, T., Buylaert, J.-P., Lu, H., Thiel, C., Murray, A., Frechen, M., … Zeng, L. (2016). Mass accumulation rate and monsoon records from Xifeng, Chinese Loess Plateau, based on a luminescence age model: Monsoon Records from Chinese Loess Plateau. *Journal of Quaternary Science*, *31*(4), 391–405. doi: 10.1002/jqs.2848

Stevens, T., Lu, H., Thomas, D. S. G., & Armitage, S. J. (2008). Optical dating of abrupt shifts in the late Pleistocene East Asian monsoon. *Geology*, *36*(5), 415. doi: 10.1130/G24524A.1

Sun, Y., Clemens, S. C., Morrill, C., Lin, X., Wang, X., & An, Z. (2012). Influence of Atlantic meridional overturning circulation on the East Asian winter monsoon. *Nature Geoscience*, *5*(1), 46–49. doi: 10.1038/ngeo1326

Thomsen, K. J., Bøtter-Jensen, L., Denby, P. M., Moska, P., & Murray, A. S. (2006). Developments in luminescence measurement techniques. *Radiation Measurements*, *41*(7), 768–773. doi: 10.1016/j.radmeas.2006.06.010

Thomsen, K. J., Murray, A. S., Jain, M., & Bøtter-Jensen, L. (2008). Laboratory fading rates of various luminescence signals from feldspar-rich sediment extracts. *Radiation Measurements*, *43*(9), 1474–1486. https://doi.org/10.1016/j.radmeas.2008.06.002

Timar-Gabor, A., Buylaert, J.-P., Guralnik, B., Trandafir-Antohi, O., Constantin, D., Anechitei-Deacu, V., Jain, M., Murray, A. S., Porat, N., Hao, Q., & Wintle, A. G. (2017). *Radiation Measurements*, *106*, 464–471. https://doi.org/10.1016/j.radmeas.2017.01.009

Wang, L., Jia, J., Zhao, H., Liu, H., Duan, Y., Xie, H., Zhang, D. D., & Chen, F. (2019)a. Optical dating of Holocene paleosol development and climate changes in the Yili Basin, arid central Asia. *The Holocene*, *29*(6), 1068–1077. https://doi.org/10.1177/0959683619831432

Wang, L., Jia, J., Xia, D., Liu, H., Gao, F., Duan, Y., Wang, Q., Xie, H., & Chen, F. (2019)b. Climate change in arid central Asia since MIS 2 revealed from a loess sequence in Yili Basin, Xinjiang, China. *Quaternary International, 502*, 258–266. https://doi.org/10.1016/j.quaint.2018.02.032

Wintle, A. G., & Murray, A. S. (2006). A review of quartz optically stimulated luminescence characteristics and their relevance in single-aliquot regeneration dating protocols. *Radiation Measurements*, *41*(4), 369–391. doi: 10.1016/j.radmeas.2005.11.001

Youn, J. H., Seong, Y. B., Choi, J. H., Abdrakhmatov, K., & Ormukov, C. (2014). Loess deposits in the northern Kyrgyz Tien Shan: Implications for the paleoclimate reconstruction during the Late Quaternary. *Catena*, *117*, 81–93. doi: https://doi.org/10.1016/j.catena.2013.09.007

Zhang, J. F., & Zhou, L. P. (2007). Optimization of the 'double SAR' procedure for polymineral fine grains. *Radiation Measurements*, *42*(9), 1475–1482. doi: 10.1016/j.radmeas.2007.06.007

Zhang, J.-F., Fan, C.-F., Wang, H., & Zhou, L.-P. (2007). Chronology of an oyster reef on the coast of Bohai Bay, China: Constraints from optical dating using different luminescence signals from fine quartz and polymineral fine grains of coastal sediments. *Quaternary Geochronology*, *2*(1), 71–76. doi: 10.1016/j.quageo.2006.05.027